Design and Optimization of the Delta-Shape Interior Permanent Magnet Synchronous Motor for Electric Vehicle Application

Sepideh Nasr[1], Babak Ganji[1*], *Senior Member, IEEE*, Mehdi Moallem[2], *Senior Member, IEEE*

[1]Faculty of Electrical and Computer Engineering, University of Kashan, Kashan, Iran

[2]Faculty of Electrical and Computer Engineering, Isfahan University of Technology, Isfahan, Iran

Email addresses: s.nasr@alumni.iut.ac.ir, bganji@kashanu.ac.ir, moallem@cc.iut.ac.ir

Abstract: Nowadays, many researchers focus on the use of clean energy instead of fossil fuels. The utilization of electric vehicles (EVs), in addition to reducing fuel consumption and associated costs and minimizing environmental pollution, allows for the recovery of a significant amount of energy. Another crucial advantage is the reduction of noise emissions when using EVs. The selection of an efficient electric motor with high power plays a vital role in EV applications. Also, the modeling process is growing more complicated as the need for greater efficiency, higher power density, and lower costs drives motors toward higher speeds and more compact designs. Consequently, interactions across multiple physical domains such as electromagnetic, thermal, and structural must be considered, even during the early stages of design. In this paper, a design algorithm is introduced for the delta-shaped interior permanent magnet synchronous motor (IPMSM), facilitating the completion of the motor's initial design. The design optimization of this type of IPMSM for EV application is also considered. The motor's performance, demagnetization, mechanical stress, and thermal performance are evaluated using the finite element method (FEM). Based on the optimized design criteria, a suitable design can be chosen from the best set of designs obtained.

Keywords: ***Interior permanent magnet synchronous motor, design optimization, electric vehicle, multi-physics simulation model, finite element method***

1. Introduction

The automotive sector has directed its attention toward enhancing the performance of electric drivetrains, aiming to encourage consumer acceptance of electric and hybrid vehicles. This focus involves considering system-wide aspects such as extending vehicle range or reducing battery mass, all with the overarching objective of reducing overall system costs. Throughout this endeavor, the choice for traction electric machines has leaned heavily toward Permanent Magnet Synchronous Motors (PMSMs). The high-efficiency PMSMs have no excitation loss, which reduces copper loss and enhances efficiency [1,2]. These electric motors are widely used in EVs due to their many advantages such as high efficiency, high power/torque density, and wide-speed operation [3]. For traction applications, the weight and size of the electric motor are also crucial factors. Among diverse types of PMSMs, the Interior Permanent Magnet (IPM) motors have advantages over Surface Permanent Magnet (SPM) motors. These advantages include better mechanical safety, higher speed, larger torque, and higher efficiency [4].

The most crucial factor affecting the performance of an IPM is the rotor shape. Therefore, determining an appropriate rotor shape for EV applications is essential [5]. Consequently, the sustainability of traction electric machines has become a key concern, prompting all vehicle manufacturers to adopt IPM synchronous machines that rely on rare-earth and heavy rare-earth materials for production vehicles. Despite the availability of diverse options, the IPMSM remains the predominant choice among traction electric machines, underscoring its widespread utilization. In [6], five types of IPM rotors for EV applications were analyzed, and the results show that the delta-shape has the highest torque compared to other topologies. The results in [7] suggest that the double-layer PMs topology has a stronger anti-demagnetization ability and wider high efficiency. In addition, to mitigate stress concentration and reduce eddy current losses, the PM pole is divided into multiple PMs [8]. The core loss of PMSM with a double-layer PMs topology structure is lower than that of a single-layer PMs topology structure at high speed. Therefore, a PMSM with a double-layer PMs is superior to the one with a single-layer PMs topology in terms of high efficiency [7]. Four different topologies of PMSMs with the same sizing are compared in [9], and it is concluded that the V-shape and delta-shape configurations have the highest output torque. Due to the significant advantages of the delta-shape IPM, such as high efficiency compared to other models by minimizing harmonic waves, the torque ripple can also be reduced, leading to less noise [10]. Therefore, this paper will delve into the design aspects of such machines.

Traditional electric motor design often prioritizes electromagnetic performance, neglecting other crucial factors. While aspects like demagnetization, thermal, and structural analysis are individually addressed, a unified design approach is lacking. Several factors must be considered, such as rotor mechanical strength and dynamics, electromagnetic fields, energy losses, and temperature management [11]. Unfortunately, the heat generated by iron losses in the rotor can only be dissipated through radiation, leading to a rise in rotor temperature and potentially causing irreversible demagnetization of the PMs [12]. Thermal analysis plays a critical role because electrical insulation has temperature limitations, and the cooling system significantly impacts performance. Cooling options include natural air, forced air, and forced coolant methods [13,14]. With the increase in volume and power level of the IPMSM, the larger-diameter PM rotor must withstand higher centrifugal forces [15]. The centrifugal force acting on the rotor results in deformation which increases with the motor speed [16,17]. The safety factor of the motor for vehicles should be generally designed to be 1.2 or more [18,19].

This paper proposes a comprehensive design method for an 80-kW, 8-pole, 4000-RPM delta-shaped IPMSM used in electric vehicles, considering structural, thermal, and demagnetization limitations. The design targets a mechanical safety factor of at least 1.2 and an efficiency exceeding 95%. Structural optimization is achieved by modifying key rotor parameters, such as bridge thickness and magnet post size. These parameters influence both electromagnetic and structural stability. The remainder of the paper is organized as follows: The design algorithm related to the delta-shape IPMSM is clearly described in Section 2. Using the described design algorithm and the proposed design optimization procedure, a delta-shape IPMSM is designed and optimized for EV application and the results are presented in Section 3. Finally, Section 4 highlights the main contributions and conclusions of the paper.

2. The design algorithm

A design algorithm for the delta-shape IPMSM depicted in Fig. 1 is described herein, allowing someone to perform the initial design of the motor. The design algorithm comprises two distinct parts: 1) Determination of the main dimensions of the machine, illustrating the machine volume, and 2) Finding all geometric parameters of the machine. These two parts are explained in the following.

(Please insert Figure 1 here)

2.1. The main dimensions of design

The initial step involves clearly defining the motor's desired performance characteristics. This includes factors such as power output, torque, speed range, operating voltage, and efficiency. The design process starts with initial assumptions for parameters like current density, air gap flux density and power factor. The diameter of the stator bore, and the stack length of the machine are defined as the main dimensions of the design and how to determine them for the IPMSM are explained in this section. An initial analytical equation, linking the rotor volume to the machine's electric and magnetic loading, serves as the foundational step in electromagnetic design [20]. The main dimensions can be calculated using the output equation of AC machines equation as follows:

$$S = \frac{P_{out}}{\eta \cos\varphi} = C_0 D^2 L n_s \tag{1}$$

where S is the rating KVA of the machine, P_{out} is the rated output power, η is efficiency, C_0 is the output power coefficient, D is the diameter of stator bore, L is the stack length of the machine and n_s is the synchronous speed. The output power coefficient is obtained using below equation:

$$C_0 = 1.1\pi^2 K_w B_{av} ac \times 10^{-3} \tag{2}$$

where K_w is winding factor, B_{av} is the specific magnetic loading and ac is the specific electric loading. The specific electric loading can be selected between 35-65 KA/m for PMSMs without cooling and it is higher for water-cooled non-salient pole synchronous machines with water direct water cooling [21-23]. The specific magnetic loading is defined as the average value of flux density over the rotor surface, and it is for a sine-distributed flux as follows [23].

$$B_{av} = \frac{2}{\pi} B_{g,\,peak} \tag{3}$$

where $B_{g,peak}$ is the peak value of flux density in the airgap. For the PMSMs, the air gap flux density (B_g) changes between 0.8 T and 1.05 T [23]. By selecting the values of magnetic and electrical loadings, the motor volume (D^2L) can be derived from (1) because other parameters are known for a specific IPMSM whose design is supposed to be completed. To separate the main dimensions (D and L), another equation is required. For this purpose, the ratio of L/τ is usually used in which τ is the pole pitch. This ratio is between 1 and 3 for the salient pole type [24]. It must be noted that the pole pitch is related to D using below equation:

$$\tau = \frac{\pi D}{P} \tag{4}$$

where P is the number of poles.

2.2. Other design parameters

After determining the main dimensions, the next step is selecting other key design parameters. These include the number of poles and slots, stator and rotor dimensions, air gap length, and winding configuration. Based on these initial choices, the preliminary electromagnetic design is conducted by calculating the stator yoke thickness, stator tooth width, stator tooth height, number of winding turns, current density, winding diameter, and the dimensions and positioning of the permanent magnets to achieve the desired torque and flux characteristics. Once the preliminary electromagnetic design is completed, structural design considerations are incorporated. This involves verifying the mechanical robustness of critical components such as the flux barrier layout, shaft, and rotor core. FEM simulations are then performed to analyze the electromagnetic performance.

Based on the initial FEM results, an adjustment phase follows, during which key design parameters are refined to improve performance. Adjustments may include optimizing the flux barrier design and modifying magnet dimensions to enhance torque production while minimizing torque ripple. Next, mechanical FEM analysis is performed to assess the motor's structural integrity, ensuring that stresses and deformations remain within acceptable limits at maximum operating speeds. Thermal analysis is then conducted to evaluate temperature distribution within the motor, ensuring that the permanent magnets, stator windings, and other components operate within safe thermal limits to maintain reliability and efficiency. If the results of the electromagnetic, structural, or thermal analyses are unsatisfactory, previous design steps are revisited, and necessary adjustments are made. Once all electromagnetic, mechanical, and thermal requirements are satisfied, the design process is considered complete. This structured and iterative approach ensures a balanced design with optimized performance, mechanical strength, and thermal stability, making it suitable for EV applications.

2.2.1. Airgap length

The air gap length is chosen based on mechanical constraints. A larger airgap reduces reluctance torque, while a smaller airgap can lead to higher-order harmonics. Once cooling type and machine dimensions are fixed, current densities can be determined. The air gap length in an IPM motor is comparable to that in an induction motor. The air gap length is typically between 0.6 and 1 mm for traction machines [25].

2.2.2. Rotor design parameters

The NdFeB-type PMs are commonly used for EV applications and therefore are considered here. The length of the PM is equal to the length of the rotor and its thickness is determined to reduce the risk of demagnetization [26]. So, the thickness of PMs could be selected 5 to 10 times larger than the air gap length for the initial design [27,28]. A wider magnet may potentially result in a larger magnetic flux density and higher torque production, but it may also lead to increased torque ripple and demagnetization risk [29]. The PMs can be demagnetized during motor operation, especially during field-weakening. High demagnetizing fields can interact with the PM's field and cause irreversible demagnetization. Temperature rise is another factor that can contribute to demagnetization. Thermal analysis is crucial to ensure PM temperatures remain within limits. If demagnetization occurs, increasing the distance between the magnet and air gap or increasing the V-angle are possible solutions [30]. As the number of PM layers increases, efficiency also increases. According to [7], the PMSM with double-layer PMs is obviously superior to the one with single-layer PMs in the proportion of high-efficiency interval. Therefore, it has been considered in the present paper. Increasing the V-angle improves torque at low speeds but reduces field-weakening capability. An appropriate angle should be chosen to meet the requirements for torque and constant power speed range [30]. In the study [31], the angle in the proposed IPMSM design was adjusted from 70° to 110°. Increasing the angle achieves the highest torque per PM volume, smoother torque ripple, and the lowest PM cost.

The concept of flux barriers in IPMSMs plays a crucial role in enhancing performance by reducing magnetic flux leakage and increasing torque. Flux barriers are strategically designed structures that help manage the magnetic field within the motor, leading to significant operational benefits [32]. The circle flux barriers are applied to reduce the mechanical stress concentration and to decrease the torque ripple.

2.2.3. Stator design parameters

A higher number of pole pairs results in a shorter end winding, meaning lower copper loss. However, this increases the fundamental frequency, leading to higher iron-core loss and switching frequency for the power electronic converter.

For the EV application, the 8-Pole 48-Slot (8P48S) and 10-Pole 45-Slot (10P45S) arrangements are commonly used, e.g., Toyota Prius 2004, Camry 2007, Honda Accord 2014, Lexus LS 600h 2008, and BEV Nissan Leaf 2011 [24]. In the present paper, the design of the 8P48S PMSM is considered because this configuration is most popular.

The stator configuration involves selecting the conductors and determining the slot/pole arrangement. The choice of the machine's pole number (P) relies on factors such as the operating speed, the drive's maximum switching frequency, available DC link voltage, and constraints related to core loss. Additionally, the winding arrangement and stator structure influence the rotor's pole numbers by considering suitable winding factors. However, higher pole numbers increase leakage flux, causing challenges such as reduced power factor and torque density in extremely high pole machines (for instance, those with $P > 16$).

Selecting a slot/pole combination considers multiple performance aspects such as noise, winding design, back-emf harmonics, torque ripple, and fundamental frequency. The winding distribution is often characterized by the parameter q, representing the number of slots per pole per phase [33]. Generally, $q = 2$ strikes a balance between average torque, losses, and moderate harmonics, commonly found in commercially available vehicles. A higher q design offers more sinusoidal back-emf, lower PM loss, and higher average torque, yet it results in higher conductor loss and thinner teeth, leading to increased core loss compared to $q = 2$.

To estimate the overall size of the machine, we can use a typical value of the split ratio, the ratio of the rotor diameter to the stator diameter. For the interior rotor PM machines, this ratio is typically about 0.6 [23]. Knowing the split ratio, the stator yoke diameter depicted with D_s on Fig. 1 can be determined because the rotor diameter (D) has already been calculated as the main dimensions in section 2.1.

The thickness of stator yoke depicted with W_{sy} on Fig. 1 can be obtained using below equation [34]:

$$W_{sy} = \frac{B_g \pi D}{B_{sy} P} \tag{5}$$

where B_{sy} is the flux density in stator yoke. For the salient pole synchronous machines, the stator yoke flux density is in the range of 1 T to 1.5 T [21]. The width of stator tooth (W_t) is obtained using below equation [35]:

$$W_t = \frac{B_g \pi D}{B_t s} \tag{6}$$

where s is slot number and B_t is the flux density in stator tooth. For the non-salient pole synchronous machines, [23] indicates that the tooth flux density is between 1.5 T and 2 T. As discussed above, the lower half of this range should be considered here. With regard to Fig. 1, the height of stator tooth (d_s) can be derived from other parameters using below equation:

$$d_s = \frac{D_s}{2} - \frac{D}{2} - g - W_{sy} \tag{7}$$

2.2.4. Stator winding

Regarding the winding design, the choice between series or parallel connections among conductors depends primarily on the available DC link voltage and the rated speed. Series connections require the phase current to pass through each conductor, leading to an increase in conductor size to maintain constant current density. In contrast, having more parallel paths reduces current and conductor size for the same current density. Additionally, parallel winding connections reduce unbalanced magnetic pull compared to the series arrangement [36-38]. For the distributed winding, the total winding factor is obtained using the following equation [23]:

$$K_w = \sin\left(\frac{y}{y_Q}\frac{\pi}{2}\right)\frac{\sin\left(\frac{\pi}{2m}\right)}{q\ \sin\left(\frac{\pi}{2mq}\right)} \tag{8}$$

where m is the number of phases, y_Q represents the slots per pole and y is expressed as the number of slot pitches. The line-line rms voltage and line current are given by [25]:

$$I_L = \frac{P_{\max}}{\sqrt{3} \times V_{LLrms} \times pf \times \eta} \tag{9}$$

The motor was designed with eight poles and $q = 2$ resulting in 48 slots for a three-phase machine. The number of turns per phase can be obtained using below equation:

$$N_{ph} = \frac{V_{ph}}{4.44\ f\ K_w \varphi_m} \tag{10}$$

where V_{ph} is phase voltage and φ_m is the maximum flux. The area and diameter of each conductor are calculated using the following equations:

$$A_z = \frac{I_{ph}}{J_c} \tag{11}$$

$$d_c = \sqrt{\frac{4A_z}{\pi}} \tag{12}$$

3. Simulation results

3.1. The initial design

Using the design algorithm described in section 2, the design of an 80-kW, 4500-RPM, 8-pole delta-type IPMSM whose specification is given in Table 1 is presented in this section. Based on (2), D^2L is obtained as 0.0027 m³. The ratio L/τ is assumed to be 3, and consequently, D and L are 132 mm and 160 mm, respectively. The initial estimation of PM thickness is about 5-10 times larger than the air gap length. By selecting an air gap of 1 mm, the thickness of the two layers of the magnet in the initial design can be considered as 3.8 mm and 2.6 mm. The number of rotor poles and stator slots is matched to eight poles and 48 slots with the distributed windings aiming to reduce the fifth and seventh harmonics. Due to physical limitations in accommodating eight poles and considering the flux barriers, as well as avoiding narrow bridge thickness in layer 2, the best choice for the initial design is a V-angle of 124° with a magnet width of 21.33 mm.

(Please insert Table 1 here)

The thickness and width of the stator yoke are obtained using (5) and (6), which are 12.2 mm and 4.1 mm, respectively. Based on (7), the slot depth is determined, and it is 21 mm. Using (8) to (10), the number of turns per phase is calculated which is 48. It should be noted that the number of conductors in each slot is assumed to be 6, and the number of parallel paths is equal to 2. The area and diameter of each conductor could be derived from (11) and (12). All obtained design parameters are listed in Table 2. To verify the proposed IPMSM, it is simulated using ANSYS Maxwell software and the predicted torque waveform is shown in Fig. 2. As it is clear from this figure, the designed motor can achieve the required torque. In the next section, structural and thermal analyses of the proposed IPMSM are carried out using the ANSYS Motor CAD software. Based on the optimal design criteria, an appropriate design can be then selected.

(Please insert Figure 2 here)

Fig. 3 presents the magnetic flux density distribution within the IPMSM under rated load conditions. The plot indicates that the maximum flux density reaches approximately 2.2 T, mainly localized around the rotor core and the edges of the N30UH magnets. No significant magnetic saturation is observed in the stator teeth or rotor yoke, confirming that the magnetic design, utilizing high-performance N30UH magnets, is properly sized to handle the rated torque without risk of saturation or demagnetization, ensuring efficient and reliable motor operation. Fig. 4 illustrates the efficiency map of the designed IPMSM across a range of speeds and torques and combined electromagnetic and thermal performance. It can be observed that the motor achieves efficiency greater than 90% over a wide operational range, which is crucial for electric vehicle applications to maximize driving range. The efficiency exceeds 95% at approximately 4000 rpm and 180 Nm, confirming that the motor design meets the efficiency requirements necessary for traction applications and aligns with the requirements in Table 1.

(Please insert Figure 3 here)

(Please insert Table 2 here)

(Please insert Figure 4 here)

3.2. Some other analyses

A structural optimization process was conducted on the motor design to ensure the safety factor is defined as [18]:

$$SF = \frac{\sigma_y}{\sigma_{max}} \tag{13}$$

where σ_y represents the yield stress, the point at which the material starts to undergo inelastic or permanent deformation, and σ_{max} is the maximum stress experienced by the rotor during rotation. The ratio of yield stress to maximum stress on rotor laminations should be no less than 1.2. Achieving maximum efficiency and power factor, the design must be optimal in terms of the rotor's mechanical and electromagnetic properties to balance performance, durability, and thermal stability under operational conditions. While maintaining a constant average torque at base speed, the bridge thickness (t_b) for the first layer and magnet post thickness (t_m) for the second layer were varied. The bridge's thickness is crucial for maintaining the mechanical integrity of the rotor. It helps distribute the mechanical stress that arises during operation, particularly under high torque conditions. Additionally, the magnet post thickness provides the necessary support for the magnets, ensuring they remain securely in place during operation.

To evaluate the influence of rotor design parameters, a parametric analysis was conducted by systematically varying t_b and t_m, both of which affect the electromagnetic and mechanical behavior of IPMSMs. The parameter t_b was primarily varied in layer 1 to address its critical role in withstanding centrifugal forces and mitigating magnetic saturation near the airgap, where flux density and mechanical stress are highest during high-speed operation. In contrast, t_m was varied in layer 2, where it governs the flux linkage between the arms of the V-shaped magnets, influences saliency, and affects reluctance torque performance. These parameters are illustrated in Fig. 5.

The minimum and maximum values of t_b and t_m were selected based on practical design constraints, including physical limitations and the available space to accommodate structural features within the rotor. To cover a meaningful range of design scenarios, seven representative models were selected. In Designs 1–4, t_b was held constant while t_m was varied to study the effect of magnet post thickness. In Designs 1 and 5–7, t_m was fixed and t_b was varied to isolate the influence of bridge thickness. This combination of parameters enabled a systematic investigation of trade-offs among key performance metrics, including efficiency, power factor, mechanical safety, and saliency ratio. Table 3 lists the design configurations considered in this study.

(Please insert Table 3 here)

(Please insert Figure 5 here)

3.2.1. Electromagnetic analysis

The effects of varying machine parameters are shown in Fig. 6. When the bridge thickness is decreased while keeping the magnet post thickness constant, the coupling between the permanent magnet flux and the stator increases. This is because the flux leakage of the magnet decreases, leading to a higher average air gap flux. As the bridge thickness decreases, the d-axis inductance decreases, and the q-axis inductance increases. This results in an increase in both magnet torque and reluctance torque for the same current. Additionally, the power factor improves due to the higher airgap flux density and reduced d-axis inductance. Based on electromagnetic analysis, design 5 is considered the best choice among designs 1, 5, 6, and 7 in terms of efficiency, power factor, and saliency ratio. When the magnet post thickness is reduced, the magnet posts become saturated more easily, and more permanent magnet flux interacts with the stator. This saturation causes an increase in d-axis reluctance and a decrease in q-axis reluctance due to the longer iron path.

3.2.2. Demagnetization study

The operation of the PM motor consistently falls within the negative d-axis domain. As a result, the PMs experience demagnetizing flux from the stator. A PM is demagnetized if its operating point drops below the knee point on the normal curve, which leads to a decrease in the remnant flux density of the PM. The goal of the optimal design is to ensure that PM demagnetization does not occur.

In the considered design process, the simulations have been conducted at a magnet temperature of 65° under the application of short circuit current, and a demagnetization study was performed. The findings have indicated that the operating point of the PM is positioned well before the knee point, specifically at an abscissa of 1500 kA/m. Consequently, the PM is not found to be demagnetized. Fig. 7 and 8 illustrate the field intensity of PMs and the corresponding demagnetizing normal curve, respectively.

(Please insert Figure 6 here)

(Please insert Figure 7 here)

(Please insert Figure 8 here)

3.2.3. Structural analysis

Higher speed increases the centrifugal force quadratically, which significantly increases the rotor stress distribution. In traction machines, high-speed operation is typically desired as a design target. If the stress induced by centrifugal force exceeds the maximum yield stress of the rotor, it results in PM deformation. This highlights a critical trade-off in design: a structure that is mechanically robust may not necessarily excel in electromagnetic performance. Structural analysis is carried out when the machine is rotating at the maximum speed. For instance, the design that achieves maximum efficiency (design 5), as illustrated in Fig. 6 does not correspond to the design with the highest structural stability (design 4).

When t_m is reduced, the average stress on the rotor increases, leading to a rise in the maximum stress value. Although design 4 boasts a safety factor of 2.54, it does not perform well in terms of electromagnetic efficiency and power factor. In contrast, design 5, which has a lower safety factor of 1.8, meets optimal conditions while maintaining high efficiency and power factor. The yield stress distribution and deformation characteristics in the rotor are depicted in the relevant Fig. 9 and Fig. 10, respectively.

3.2.4. Thermal analysis

Since design 5 was identified as a candidate in the previous analysis, it is essential to evaluate whether this model can meet the thermal limitations. A 2D-coupled electro-thermal analysis was conducted to determine if the winding and PMs in design 5 operate within their maximum allowable temperature limits. In this analysis, liquid cooling was implemented using water as the coolant, with a flow rate of 6.5 liters per minute. The thermal limit for both the winding and the PMs is set at 180 °C. The results indicated that the maximum temperature of the magnets reached 125 °C, while the winding temperature was found to be 142 °C, as illustrated in Fig. 11. This analysis confirms that design 5 operates within the thermal limits, ensuring both the winding and magnets remain below their maximum allowable temperatures. As a result, the output torque simulated in ANSYS for the candidate model (design 5) complies with the required specifications.

(Please insert Figure 9 here)

(Please insert Figure 10 here)

(Please insert Figure 11 here)

4. Conclusion

A comprehensive design approach was developed for a high-power delta-type IPMSM, used in electric vehicles, with all critical electromagnetic, structural, and thermal aspects considered. While achieving optimal electromagnetic performance was a primary goal, structural and demagnetization studies were also essential to ensure the mechanical and magnetic integrity of the motor especially under high-speed conditions typically encountered in electric vehicle applications. The structural analysis verified that the rotor could withstand high rotational speeds without exceeding material stress limits, thereby ensuring mechanical reliability and a sufficient safety factor. Similarly, the demagnetization study ensured that the permanent magnets remained stable and did not risk irreversible magnetic loss under high temperatures and demagnetizing currents. These analyses are especially crucial in EV applications, where the motor operates in demanding environments over extended lifespans. This multi-physics design addresses all critical considerations for delta-shaped IPMSMs used in EVs. A mechanical safety factor exceeding 1.2, coupled with a target maximum efficiency, was identified as the optimal design goal. Structural analysis was performed to evaluate the design. While all options met the structural criteria, the design that excelled structurally did not necessarily perform best electromagnetically. By incorporating these studies into the design process, the proposed motor not only meets efficiency and performance targets as a primary goal but also demonstrates high durability and robustness. Therefore, a candidate model was chosen for further assessment based on thermal limitations to ensure it met all constraints. Ultimately, a design that satisfied the optimal conditions was achieved. Considering more design parameters for the design optimization and using the optimization algorithms to find the optimum values of the parameters are suggested as future works.

References

1. Sun, X., Shi, Z., Cai, Y., et al., "Driving-cycle-oriented design optimization of a permanent magnet Hub motor drive system for a four-wheel-drive electric vehicle", IEEE Transactions on Transportation Electrification, 6(3), pp. 1115-1125 (2020). DOI: https://doi.org/10.1109/TTE.2020.3009396
2. Hou, L., Guo, Y., Ba, X., et al., "Efficiency improvement of permanent magnet synchronous motors using model predictive control considering core loss", Energies, 17(4), Art no. 773 (2024). DOI: https://doi.org/10.3390/en17040773
3. Nair, S.V., Layek, K., Hatua, K., "An unequal split dual three-phase PMSM with extended torque-speed characteristics for automotive application", IEEE Transactions on Power Electronics, 37(10), pp. 12437-12449 (2022). DOI: https://doi.org/10.1109/TPEL.2022.3169335
4. Abdel-Wahed, A.T., Ullah, Z., Abdel-Khalik, A.S., et al., "Design and finite-element-based optimization for a 12-slot/10-pole IPM motor with integrated onboard battery charger for electric vehicle applications", Machines, 11(5), Art no. 534 (2023). DOI: https://doi.org/10.3390/machines11050534
5. Niu, L., Zhang, M., "Rotor topology optimization and electromagnetic performance analysis of interior permanent magnet synchronous motors for electric vehicle applications", The Journal of Engineering, 2023 (2), Art no. 212240 (2023). DOI: https://doi.org/10.1049/tje2.12240
6. Hwang, M.H., Han, J.H., Kim, D.H., et al., "Design and analysis of rotor shapes for IPM motors in EV power traction platforms", Energies, 11(10), Art no. 2601 (2018). DOI: https://doi.org/10.3390/en11102601
7. Song, T., Zhang, Z., Liu, H., et al., "Multi-objective optimisation design and performance comparison of permanent magnet synchronous motor for EVs based on FEA", IET Electric Power Applications, 13(8), pp. 1157-1166 (2019). DOI: https://doi.org/10.1049/iet-epa.2019.0069
8. Du, G.H., Huang, N., Zhao, Y.Y., et al., "Comprehensive sensitivity analysis and multiphysics optimization of the rotor for a high speed permanent magnet machine", IEEE Transactions on Energy Conversion, 36(1), pp. 358-367 (2021). DOI: https://doi.org/10.1109/TEC.2020.3005568
9. Zhu, S., Hu, Y., Liu, C., et al., "Iron loss and efficiency analysis of interior PM machines for electric vehicle applications", IEEE Transactions on Industrial Electronics, 65(1), pp. 114-124 (2018). DOI: https://doi.org/10.1109/TIE.2017.2723859
10. Lakshmikanth, S., "Noise and vibration reduction in PMSM-A review", International Journal of Electrical and Computer Engineering, 2(3), Art no. 405 (2012). DOI: https://doi.org/10.11591/ijece.v2i3.322.
11. Gong, C., Li, S.F., Habetler, T., et al., "Acoustic modeling and prediction of ultrahigh-speed switched reluctance machines based on multiphysics finite element analysis", IEEE Transactions on Industrial Applications, 57(1), pp. 198-207 (2021). DOI: https://doi.org/10.1109/TIA.2020.3028318
12. Tong, W.M., Li, S.Q., Sun, R.L., et al., "Modified core loss calculation for high-speed PMSMs with amorphous metal stator cores", IEEE Transactions on Energy Conversion, 36(1), pp. 560-569 (2021). DOI: https://doi.org/10.1109/TEC.2020.3007885
13. Wang, Q., Wu, Y., Niu, S., et al., "Advances in thermal management technologies of electrical machines", Energies, 15(9), Art no. 3249 (2022). DOI: https://doi.org/10.3390/en15093249
14. Satrústegui de Legarra, M. "Thermal and hydraulic design of water-based cooling systems for electrical machines", PhD thesis, Universidad de Navarra (2018).
15. Gu, Y.X., Wang, X.Y., Gao, P., et al., "Mechanical analysis with thermal effects for high-speed permanent-magnet synchronous machines", IEEE Transactions on Industrial Applications, 57(5), pp. 4646-4656 (2021). DOI: https://doi.org/10.1109/TIA.2021.3087120
16. Greef, C.D., Kluyskens, V., Henrotte, F., et al., ''Time-efficient multi-physics optimization approaches for the design of synchronous reluctance motors'', IEEE Energy Conversion Congress and Exposition, Vancouver, BC, Canada, pp. 4197-4204 (2021). DOI: https://doi.org/10.1109/ECCE47101.2021.9595977
17. Zhang, G., Jewell, G.W., "Combined electromagnetic and mechanical design optimization of interior permanent magnet rotors for electric vehicle drivetrains", World Electric Vehicle Journal, 15(1), Art no. 4 (2024). DOI: https://doi.org/10.3390/wevj15010004
18. Jang, D., Kang, D.H., Lee, S.C., et al., "Design of wide operation area and high safety factor traction motor for electric vehicle (EV)", 24th International Conference on Electrical Machines and Systems, Gyeongju, Korea, pp. 1268-1273 (2021). DOI: https://doi.org/10.23919/ICEMS52562.2021.9634202
19. Jung, Y.H., Kim K.O., Hong, J.P., "Design of multi-layer IPMSM using ferrite PM considering mechanical and electrical characteristics", IEEE Energy Conversion Congress and Exposition, Baltimore, MD, USA, pp. 3534-3541 (2019). DOI: https://doi.org/10.1109/ECCE.2019.8912188
20. Torrey, D. A., "AC electric machines and their control", E-Man Press LLC (2010).
21. Toliyat, H.A., Kliman, G.B., "Handbook of electric motors", CRC press (2018). DOI: https://doi.org/10.1201/9781420030389
22. Jurca, F., Martis, C., "Theoretical and experimental analysis of a three-phase permanent magnet claw-pole synchronous generator", IET Electric Power Applications, 6(8), pp. 491-503 (2012). DOI: https://doi.org/10.1049/iet-epa.2012.0075
23. Pyrhonen, J., Jokinen, T., Hrabovcova, V., "Design of rotating electrical machines", John Wiley & Sons (2013). DOI: https://doi.org/10.1002/9781118701591
24. Tang, J., "Synchronous machines with high-frequency brushless excitation for vehicle applications", MSc thesis, Chalmers Tekniska Hogskola, Sweden (2019).
25. Husain, I., "Electric and hybrid vehicles: design fundamentals", CRC press (2021). DOI: https://doi.org/10.1201/9780429490927
26. Song, S.W., Pyo, H.J., Nam, D.W., et al. "Irreversible demagnetization improvement process of hybrid traction motors with Dy-free magnets", Machines, 11(1), Art no. 4 (2023). DOI: https://doi.org/10.3390/machines11010004
27. Bird, J., Lipo, T., "An electrodynamic wheel with a split-guideway capable of simultaneously creating suspension, thrust and guidance forces", University of Wisconsin-Madison (2005).
28. Hendershot, J.R., Miller, T.J.E., "Design of brushless permanent-magnet motors", Magna Physics (1994). DOI: https://doi.org/10.1093/oso/9780198593898.001.0001
29. Nishiyama, N., Uemura, H., Honda, Y., "The optimum design of the magnetic orientation of permanent magnets for IPMSM under hot environments", 12th International Conference on Power Electronics and Drive Systems, Honolulu, HI, USA, pp. 380-385 (2017). DOI: https://doi.org/10.1109/PEDS.2017.8289239

30. Veena, P., Nair, S.V., Hatua, K., “Electromagnetic, structural and thermal analysis of interior permanent magnet synchronous motor for electric vehicle application”, 11th International Conference on Power Electronics and ECCE Asia, Jeju, Korea, pp.148-153 (2023). DOI: https://doi.org/10.23919/ICPE2023-ECCEAsia54778.2023.10213690
31. Jeong, H., Baek, J., “Design of three-phase V-shaped interior permanent magnet synchronous motor for air conditioning compressor of electric vehicle”, Applied Sciences, 10(24), Art no. 8785 (2020). DOI: https://doi.org/10.3390/app10248785
32. Huynh, T.A., Nguyen Le, Y.T., Lee, Z., et al., “Influence of flux barriers and permanent magnet arrangements on performance of high-speed flux-intensifying IPM motor”, IEEE Transactions on Magnetics, 59(11), Art no. 8203606 (2023). DOI: https://doi.org/10.1109/TMAG.2023.3290538
33. Xiong, F., Yan, R., Xie, Y., et al., “Design and optimization of an interior permanent-magnet synchronous motor for aircraft drive application”, Applied Sciences, 14(1), Art no. 309 (2024). DOI: https://doi.org/10.3390/app14010309
34. Kong, Y., Lin, M., Jia, L., “A novel high power density permanent-magnet synchronous machine with wide speed range”, IEEE Transactions on Magnetics, 56(2), Art no. 7505206 (2020). DOI: https://doi.org/10.1109/TMAG.2019.2947611
35. Soleimani Keshayeh, M.J., Gholamian, S.A., “Optimum design of a three-phase permanent magnet synchronous motor for industrial applications”, International Journal of Applied Operational Research, 2(4), pp. 67-86, 2013.
36. Yang, Y., Castano, S.M., Yang, R., et al., “Design and comparison of interior permanent magnet motor topologies for traction applications”, IEEE Transactions on Transportation Electrification, 3(1), pp. 86-97 (2017). DOI: https://doi.org/10.1109/TTE.2016.2614972
37. Islam, M.S., Husain, I., Ahmed, A., et al., “Asymmetric bar winding for high-speed traction electric machines”, IEEE Transactions on Transportation Electrification, 6(1), pp. 3-15 (2020). DOI: https://doi.org/10.1109/TTE.2019.2962329
38. Kabir, M.A., “High performance reluctance motor drives with three-phase standard inverter”, PhD thesis, North Carolina State University, USA (2017).

Figure captions:

Fig. 1. The cross-section of the considered IPMSM

Fig. 2. The predicted instantaneous torque

Fig. 3. The magnetic flux density contour plot

Fig. 4. Efficiency map of the designed IPMSM across speed and torque ranges

Fig. 5. Structural parameters selected for optimization

Fig. 6. Variation of machine performance with bridge and magnet pole thickness: (a) Power factor, (b) Efficiency, (c) Saliency ratio

Fig. 7. Magnetic field intensity of magnet at operating point (65°C)

Fig. 8. Demagnetizing curve

Fig. 9. Von-mises stress distribution in rotor

Fig. 10. Deformation in rotor

Fig. 11. Temperature distribution of design 5

Table captions:

Table 1. Machine Ratings

Table 2. Design parameters

Table 3. Controllable Factors and Corresponding Values

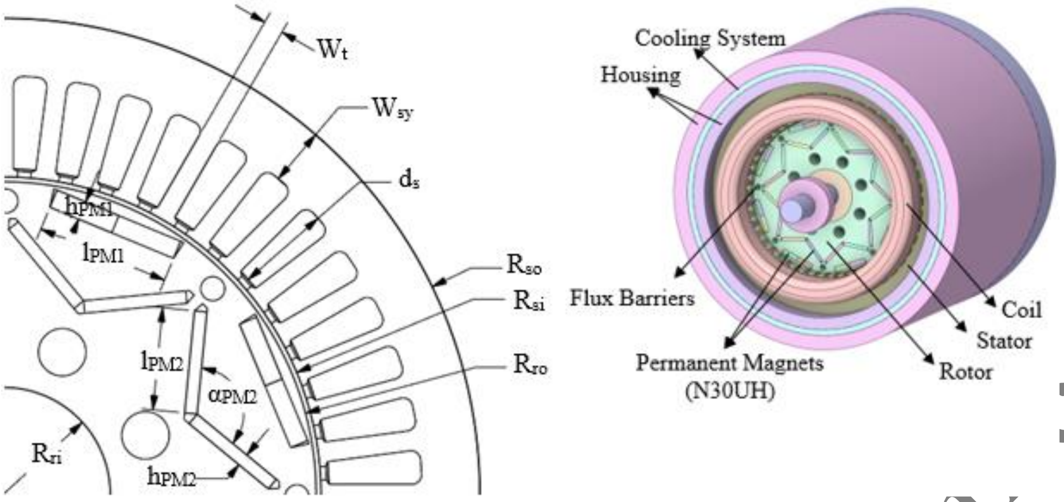

Fig. 1. The cross-section of the considered IPMSM

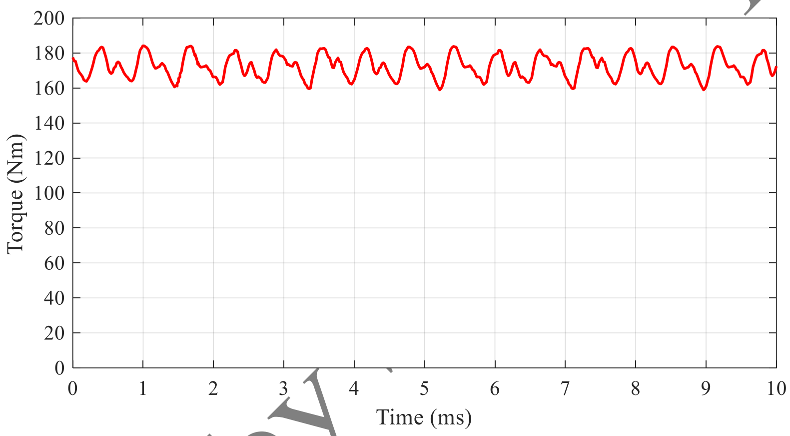

Fig. 2. The predicted instantaneous torque

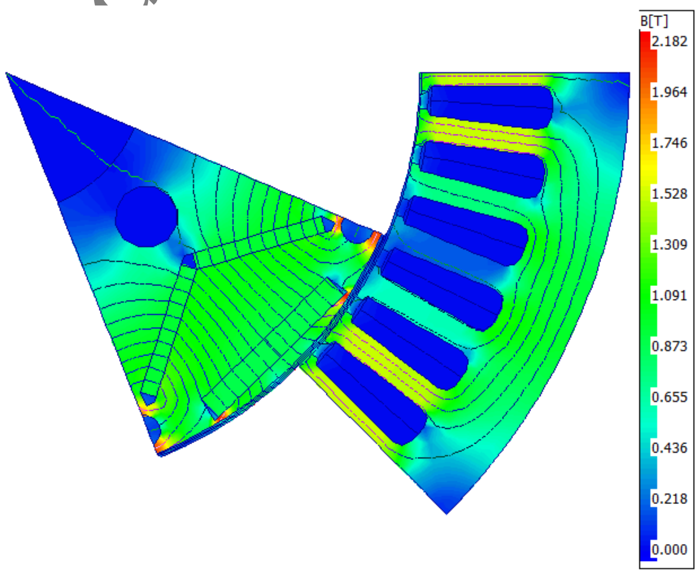

Fig. 3. The magnetic flux density contour plot

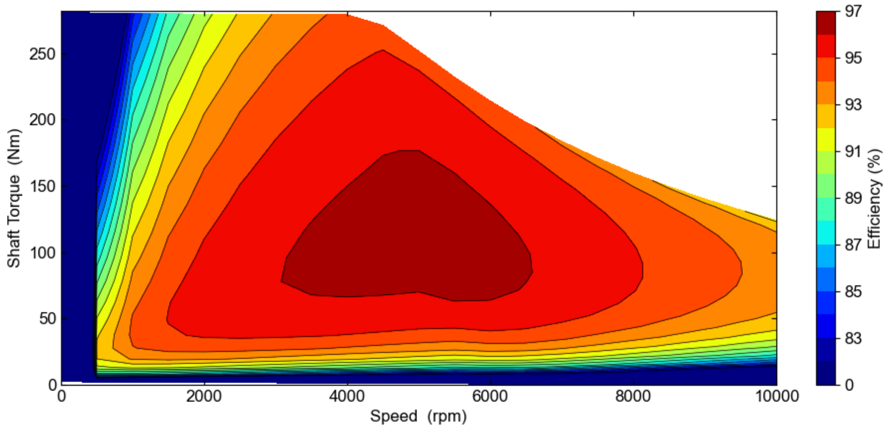

Fig. 4. Efficiency map of the designed IPMSM across speed and torque ranges

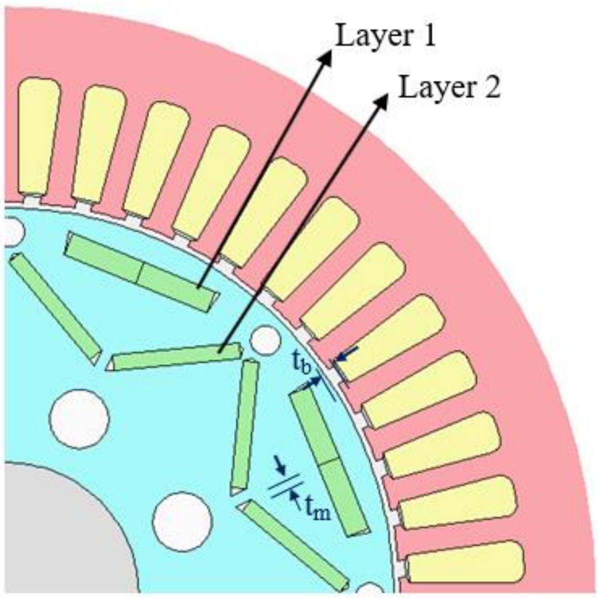

Fig. 5. Structural parameters selected for optimization

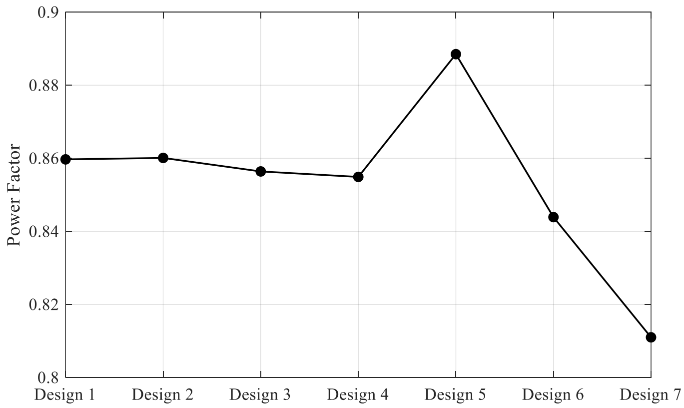

(a)

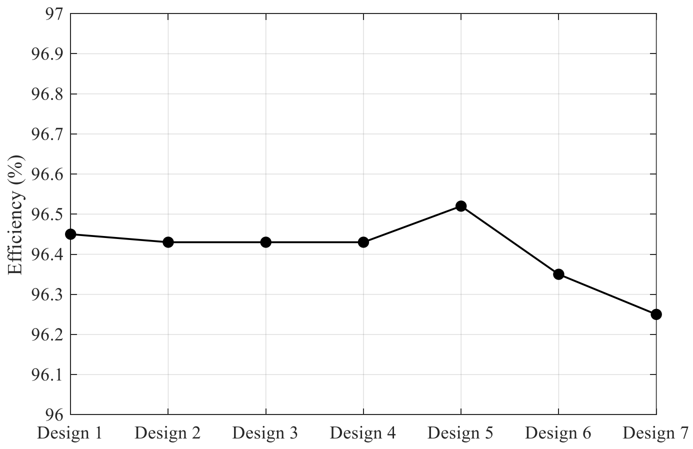

(b)

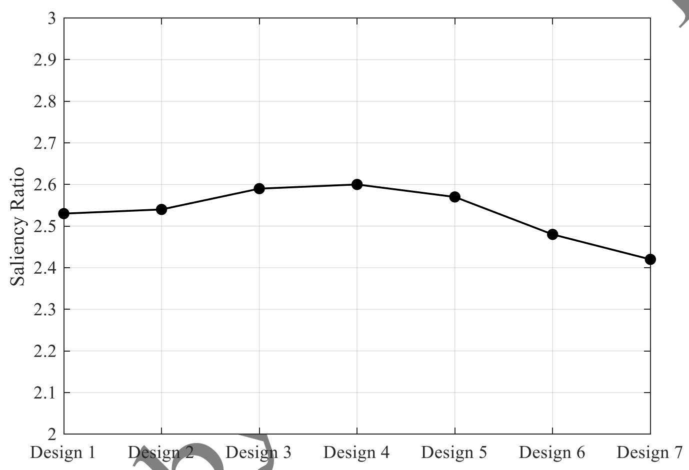

(c)

Fig. 6. Variation of machine performance with bridge and magnet pole thickness: (a) Power factor, (b) Efficiency, (c) Saliency ratio

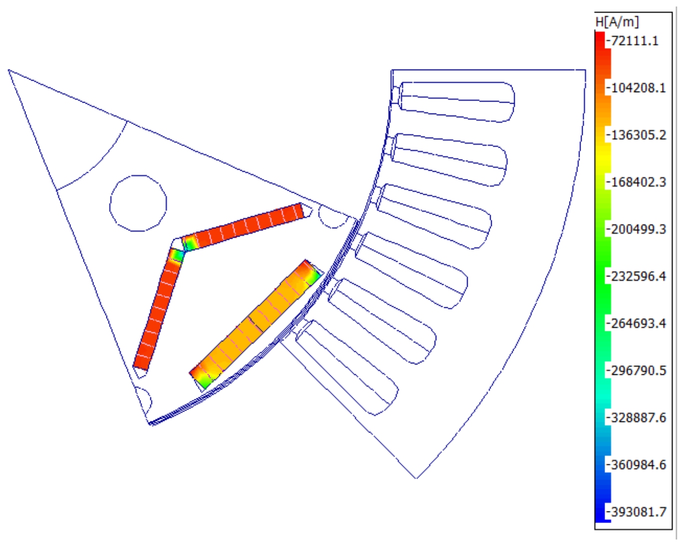

Fig. 7. Magnetic field intensity of magnet at operating point (65°C)

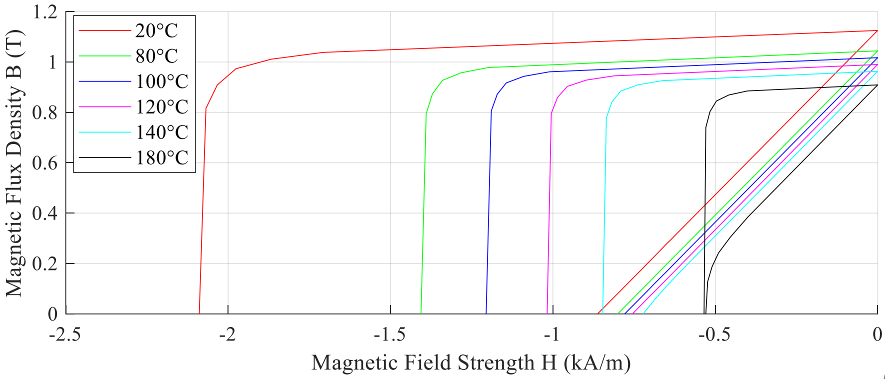

Fig. 8. Demagnetizing curve

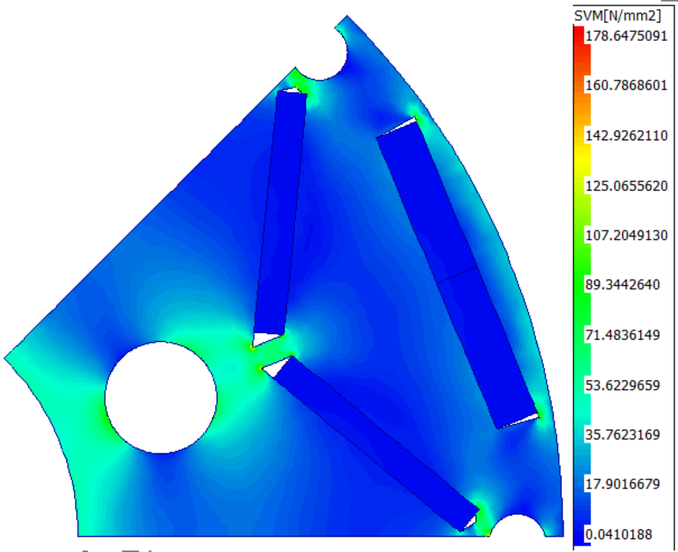

Fig. 9. Von-mises stress distribution in rotor

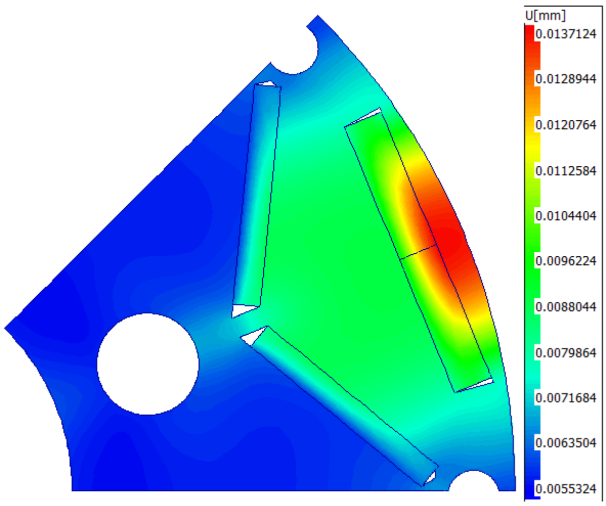

Fig. 10. Deformation in rotor

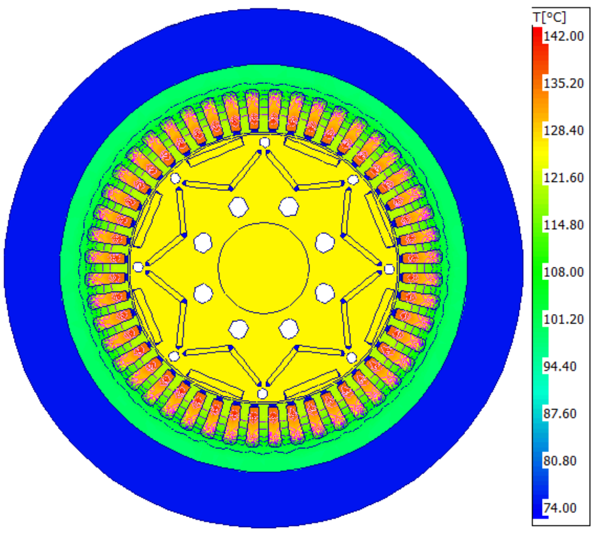

Fig. 11. Temperature distribution of design 5

Table 1. Machine Ratings

Parameter	Target
Rated power (kW)	80
Rated torque (Nm)	180
Efficiency (%)	>95
Power density (kW/L)	>5
Rated speed (rpm)	4000
Maximum speed (rpm)	10000
Maximum von-Mises stress (MPa)	370
Winding temperature (°C)	180
Magnet temperature (°C)	180
Safety factor	>1.2

Table 2. Design parameters

Parameter	Value
Outer radius of stator (R_{so})	99 mm
Inner radius of stator (R_{si})	66 mm
Outer radius of rotor (R_{ro})	65.5 mm
Inner radius of rotor (R_{si})	22.21 mm
Rotor length	150 mm
Stator length	160 mm
Air gap length	1 mm

Number of slot/Pole	48/8
Turns per phase	48
Conductors per slot	6
Slot depth (d_s)	21 mm
Slot space factor	0.4
Slot per phase	16
Yoke height (W_{sy})	12.2 mm
Tooth width (W_t)	4.1 mm
Winding factor	0.933
Wire diameter	3.1 mm
PM type	N30UH
Magnet thickness of outer layer (h_{PM1})	3.88 mm
Magnet bar width of outer layer (l_{PM1})	13.9 mm
Pole V angle of outer layer (α_{PM1})	180°
Magnet thickness of inner layer (h_{PM2})	2.6 mm
Magnet bar width of inner layer (l_{PM2})	21.33 mm
Pole V angle of inner layer (α_{PM2})	124°

Table 3. Controllable Factors and Corresponding Values

	Bridge thickness (t_b)	Magnet post thickness (t_m)
Design 1	1.2 mm	0
Design 2	1.2 mm	0.75 mm
Design 3	1.2 mm	1.5 mm
Design 4	1.2 mm	2 mm
Design 5	0.6 mm	0
Design 6	1.8 mm	0
Design 7	2.4 mm	0

Biographies:

Sepideh Nasr was born in Isfahan, Iran, in 1990. She received her M.Sc. in Electrical Engineering from the Isfahan University of Technology, Isfahan, Iran, in 2016. She is currently pursuing a Ph.D. degree in Electrical Engineering at the University of Kashan in Iran. Her main research interest includes electrical and thermal design of electrical machines, especially PMSM for EV applications.

Dr. Babak Ganji received B.Sc. degree from Isfahan University of Technology, Iran in 2000, and M.Sc. and Ph.D. from University of Tehran, Iran in 2002 and 2009, respectively, all in major electrical engineering-power. He was granted DAAD scholarship in 2006 from Germany and worked in Institute of Power Electronics and Electrical Drives (ISEA) at RWTH Aachen University as a visiting researcher for 6 months. He has been working at University of Kashan in Iran since 2009 as an Associate Professor and his research interest is modeling and design of electric machines, especially switched reluctance machine.

Prof. Mehdi Moallem (SM'95) received the Ph.D. degree in electrical engineering from Purdue University, West Lafayette, IN, in 1989. He has been with the Department of Electrical and Computer Engineering, Isfahan University of Technology, Isfahan, Iran since 1991. His research interests include design and optimization of electromagnetic devices, application of advance numerical techniques and intelligent systems to analysis and design of electrical machines, and power quality.